Manuscript
Click here to download Manuscript: NAwinterpaper_RESUB_final6.docx
Click here to view linked References

Extreme air-sea interaction over the North Atlantic subpolar gyre during the winter of 2013-14 and its sub-surface legacy

Jeremy P. Grist[1], Simon A. Josey[1]
Zoe L. Jacobs[2], Robert Marsh[2], Bablu Sinha[1], and Erik Van Sebille[3,4]

[1]National Oceanography Centre, European Way, Southampton, SO14 3ZH, UK
(jeremy.grist@noc.ac.uk; simon.a.josey@noc.ac.uk; bablu.sinha@noc.ac.uk)
[2]Ocean and Earth Science, National Oceanography Centre Southampton University of Southampton
Waterfront Campus European Way Southampton SO14 3ZH United Kingdom
(zlj1e13@soton.ac.uk; robert.marsh@noc.soton.ac.uk)
[3]Climate Change Research Centre and ARC Centre of Excellence for Climate System Science,
University of New South Wales Sydney, NSW 2052, Australia
[4]Grantham Institute & Department of Physics, Imperial College London, London, SW7 2AZ, United
Kingdom (E.van-Sebille@imperial.ac.uk)

Abstract

Exceptionally low North American temperatures and record-breaking precipitation over the British Isles during winter 2013-14 were interconnected by anomalous ocean evaporation over the North Atlantic Subpolar Gyre region (SPG). This evaporation (or oceanic latent heat release) was accompanied by strong sensible heat loss to the atmosphere. The enhanced heat loss over the SPG was caused by a combination of surface westerly winds from the North American continent and northerly winds from the Nordic Seas region that were colder, drier and stronger than normal. A distinctive feature of the air-sea exchange was that the enhanced heat loss spanned the entire width of the SPG, with evaporation anomalies intensifying in the east while sensible heat flux anomalies were slightly stronger upstream in the west. The immediate impact of the strong air-sea fluxes on the ocean-atmosphere system included a reduction in ocean heat content of the SPG and a shift in basin-scale pathways of ocean heat and atmospheric freshwater transport. Atmospheric reanalysis data and the EN4 ocean data set indicate that a longer-term legacy of the winter has been the enhanced formation of a particularly dense mode of Subpolar Mode Water (SPMW) - one of the precursors of North Atlantic Deep Water and thus an important component of the Atlantic Meridional Overturning Circulation. Using particle trajectory analysis, the likely dispersal of newly-formed SPMW is evaluated, providing evidence for the re-emergence of anomalously cold SPMW in early winter 2014/15.

1. Introduction

The boreal winter of 2013-14 brought extreme weather conditions to both north America (Palmer 2014) and northwest Europe (Mathews et al. 2014). The North American winter was notable for temperatures that were extremely low both for specific episodes and in terms of the winter-long average. On 6 January 2014, record lows in daily temperatures were set in approximately 50 cities across the US (National Aeronautics and Space Administration 2014), while for eight mid-western states the December, January and February mean temperature was in the coldest 10% of a 129 year record (National Climatic Data Center 2014). In the United Kingdom, December, January and February were the wettest in over 100 years and led to flooding of major rivers such as the Thames (Slingo et al. 2014). High levels of precipitation were accompanied by high wind speeds, and when both intensity and duration of the winter cyclones are taken into account, it was the stormiest on record for the UK and Ireland (Mathews et al. 2014). Although considerable attention has been paid to the atmospheric conditions associated with both the North American and European winters (Ballinger et al. 2014; Slingo et al. 2014; Huntingford et al. 2014; van Oldenborgh et al. 2015; Screen et al. 2015), less attention has been paid to the air-sea interaction processes that link the two.

In this paper, we analyse North Atlantic air-sea fluxes during the winter of 2013-14. We put air-sea flux anomalies of this winter in the context of recent variability, evaluate the immediately observed impact on the ocean-atmosphere system and consider the likely implications for the North Atlantic ocean-atmosphere system on seasonal-to-interannual timescales. Our analysis consists of three parts. Firstly, using atmospheric reanalysis, we determine the anomalous surface heat, freshwater and momentum fluxes along with their contributing components. In addition, the surface conditions that led to the particular patterns

of air-sea exchange are diagnosed. Secondly, we examine the immediate effect of the winter's air-sea exchange on ocean and atmospheric transport pathways and local heat storage. Thirdly, through a combined observation-model analysis, we examine the winter formation of Subpolar Mode Water (SPMW) and the potential longer-term impacts of this anomalous water mass on regional climate.

2. Data, Model and Analysis Methods

In the following sub-sections, we describe the sources and methods for the air-sea fluxes, atmospheric moisture transport, hydrographic data, water mass transformation, and water mass trajectories.

2.1 Air-sea fluxes

Our primary set of monthly air-sea flux fields come from the NCEP/NCAR atmospheric reanalysis (2.5 x 2.5º horizontal resolution) for the period April 1979 to March 2014 (Kalnay et al. 1996). The air-sea fluxes employed are net heat flux (and its components, latent heat flux, sensible heat flux, net shortwave radiation and net longwave radiation); net freshwater flux (and its components, precipitation and evaporation) and the momentum flux (wind stress). The surface turbulent heat fluxes (i.e. the sensible heat flux Q_H and the latent heat flux Q_E) can be estimated (and physically interpreted) from the following formulae:

$$Q_H = \rho c_p C_h u (T_s - T_a) \quad (1)$$

$$Q_E = \rho L C_e u (q_s - q_a) \quad (2)$$

Where ρ is the density of air; c_p, the specific heat capacity of air at constant pressure; L, the latent heat of vaporization, C_h and C_e, the stability and height dependent transfer coefficients for Q_H and Q_E respectively; u, the wind speed; T_s, the sea surface temperature; T_a, the air

temperature; q_a, the atmospheric specific humidity and q_s, 98% of the saturation specific humidity at T_s (to allow for the salinity of sea water, e.g. Josey et al. 2013). As well as considering the latent and sensible heat flux individually, we also analyse the driving variables u, T_s, T_a and the near surface gradients (T_s - T_a) and (q_s - q_a).

As well as NCEP/NCAR, further analysis was undertaken with the ERA-Interim reanalysis (Dee et al. 2011) and the Woods Hole Oceanographic Institute Objectively Analyzed Air-Sea Fluxes for the Global Ocean (OAFlux, Yu and Weller 2007). The results using these additional datasets are very similar to those using the NCEP/NCAR dataset so, to avoid undue repetition, selected ERA-Interim and OAFlux results are shown in addition to NCEP/NCAR where appropriate. For the purpose of the analysis, unless otherwise stated, the winter of 2013-14 (hereafter W14) is defined as the mean of December 2013, January 2014 and February 2014. The extent that the W14 air-sea fluxes departed from the long-term mean is examined using spatial maps. The longer-term mean here is defined as being the 35-year mean 1979-1980 to 2013-2014.

2.2 Atmospheric moisture transport

In addition to using the surface fields from the reanalysis, the tropospheric fields of wind and specific humidity are used to calculate the integrated water vapour transport (e.g. Lavers et al. 2012),

$$IVT = \sqrt{\left(\left(\frac{1}{g}\int_{1000}^{300} q u_z \, dp\right)^2 + \left(\frac{1}{g}\int_{1000}^{300} q u_m \, dp\right)^2\right)} \qquad (3)$$

where u_z and u_m are the zonal and meridional components of the wind speed (m s^{-1}) respectively, q is the specific humidity (kg kg^{-1}), p (Pa) is the atmospheric pressure and g is the acceleration due to gravity (m s^{-2}) and the transport is integrated from 1000mb to 300mb. The units of IVT are kg m^{-1} s^{-1}.

113

114 2.3 Hydrographic data and calculations

115 Monthly estimates of ocean temperature and salinity for the period January 2002 to
116 July 2014 are taken from objectively-analysed gridded fields of the EN4 dataset provided by
117 the UK Met Office Hadley Centre. From 2002, the Argo float programme provided
118 significantly improved the EN4 data coverage in the Atlantic Ocean. EN4 comprises global
119 gridded fields of potential temperature and salinity at 1º resolution with 42 vertical levels
120 (Good et al. 2013). The gridded temperature and salinity estimates were used to examine
121 changes in upper ocean heat content, changes in the vertical temperature structure and
122 changes in the zonal geostrophic flow of the North Atlantic Current. Using TEOS-10
123 software (http://www.teos-10.org/), geostrophic currents were computed from horizontal
124 density gradients according to the thermal wind relation, assuming a level of no motion at
125 1000 m.

126

127 2.4 Water mass transformation

128 In addition, the surface salinity fields were used in conjunction with the heat and
129 freshwater fluxes from the NCEP/NCAR reanalysis to estimate the water mass formation
130 rate for the eastern (i.e. east of 30º W) Subpolar Gyre of the North Atlantic. This was
131 achieved by taking the diapycnal divergence of diapycnal volume fluxes, following Walin
132 (1982), Speer and Tziperman (1992), Marsh (2000), Grist et al. (2009) and others.

133

134 2.5 Water mass trajectories

135 Water particle trajectory analyses are undertaken with hindcast datasets for 1988-
136 2007 using the 1/12th degree NEMO ocean model (Madec 2008) and for 1980-2010 using the
137 1/10th degree OFES ocean model (Masumoto et al. 2004). The NEMO simulation, which is

hindcast ORCA0083-N001 in the DRAKKAR data set of simulations (Barnier et al. 2006; DRAKKAR-Group, 2007), is referred to as ORCA12 in this paper. Further details of ORCA12 are documented in Duchez et al. (2014). The Ocean General Circulation Model for the Earth Simulator (OFES) spans 75°S to 75°N, and is forced with a combination of data from the NCEP/NCAR reanalysis. Within both models, virtual particles representative of selected anomalous mode water in the eastern SPG are advected using the three-dimensional velocity fields, at five-day resolution for ORCA12 and three-day resolution for OFES. ARIANE software (Blanke and Raynaud 1997) is used to calculate trajectories in ORCA12 in a manner similar to Grist et al. (2014). The Connectivity Modelling System (CMS) v1.1 (Paris et al. 2013) is used to calculate the trajectories in OFES. By using two different particle-tracking methods with model output from two different eddy-resolving hindcasts, agreement in the derived Lagrangian statistics increases confidence in our conclusions regarding the short-term transport and mixing of anomalous mode water.

3. Results

3.1 Anomalous Air-Sea Fluxes During Winter 2013-14

We first examine the extent that W14 air-sea fluxes of net heat, freshwater and momentum differed from the long-term mean. We then examine the flux components and the surface terms that caused the anomalous fluxes.

3.1.1 Net Heat, Freshwater and Momentum Fluxes

Anomalous air-sea fluxes of net heat, freshwater (precipitation minus evaporation) and momentum (surface wind stress) for W14 from the NCEP/NCAR atmospheric reanalysis are shown in Fig. 1. The period was characterized by anomalously strong heat loss (Fig. 1a) over the subpolar region. In particular, over the eastern subpolar gyre (SPG) (30º W - 20º W,

40º N - 50º N) heat loss was more than 110 Wm^{-2} (or three standard deviations) greater than the long-term mean. In the subtropical gyre, the W14 heat fluxes were anomalously weak (strong) heat loss in the western (eastern) half of the basin. Although these subtropical anomalies formed coherent large-scale patterns, they were not of the extreme levels that occurred in the subpolar region.

The field of anomalous net freshwater surface flux (Fig. 1b) for W14 indicates two regions of significant increase in ocean freshwater gain; one in the south-western subtropical gyre (STG) (80º W- 60º W, 25º N – 30º N) and the other in the eastern SPG (20º W -10ºW, 50ºN to 60ºN), slightly to the north of the region of the greatest anomalous heat flux. The latter region is in contrast to the western SPG/Labrador Sea, where there was increased net evaporation. Considering the prevailing west-east passage of mid-latitude storms, the pattern suggests an atmospheric transfer of freshwater from the western to the eastern SPG. The other significant net freshwater flux anomaly in the North Atlantic during W14 was increased net evaporation in the central STG (40º W -30º W, 30º N – 40º N). This feature is consistent with the stronger surface easterlies implied by the enhanced subtropical heat flux in Fig. 1a and seen in Fig.1d.

The field of anomalous W14 momentum flux is dominated by a band across the Atlantic between 45ºN and 55ºN where the flux is up to 0.2 Nm^{-2} greater than normal. The anomaly is greater and more significant in the eastern half of the basin. The east-west band corresponds with the southern side of the track of a series of unusually well clustered mid-latitude storms (Slingo et al. 2014). The northern flank of the passage of these storms is also characterized by enhanced momentum flux between 40ºW and 20ºW and 60ºN and 70ºN.

In summary, the strongest W14 surface flux anomalies were in the net heat flux and the momentum flux over the SPG, with particularly enhanced fluxes over the eastern half of

187 the basin. We now examine the anomalies of the different components of the heat and
188 freshwater fluxes, with a particular emphasis on the subpolar (or mid-latitude) region where
189 the largest anomalies are evident.
190
191 3.1.2 Components of the surface heat flux
192 The anomalous components of the W14 net heat flux, that is the latent heat flux,
193 sensible heat flux, net shortwave radiation and net longwave radiation are shown in Fig. 2. It
194 is clear from the figure that the turbulent fluxes (latent and sensible heat) dominate the
195 increase in the oceanic heat loss over the mid-latitude band, with the anomalous radiative
196 fluxes (Fig. 2 c and d) contributing relatively little. Both the latent and sensible heat loss
197 anomalies occupy similar areas stretching from the Labrador Sea in the west to the north–
198 eastern tip of the Iberian Peninsula in the south-east and the Rockall Trough in the north-east.
199 The significance of both the turbulent fluxes is greater in the eastern half of the basin, where
200 the anomalies are more than three standard deviations from the long-term mean. However the
201 strength of the sensible heat anomaly is greater in the west, with anomalies peaking at -54
202 Wm^{-2} at 47 ºW, 50ºN, compared with a peak of -67 Wm^{-2} at 20 ºW, 50ºN in the latent heat
203 flux.
204 Similar results are obtained when alternative datasets (ERA-Interim and OAFlux) are
205 considered, thus indicating that our conclusions are not sensitive to the choice of flux
206 product. First, the anomalous net heat flux for W14 from ERA-Interim together with the
207 associated sea level pressure and wind fields are shown in Fig. 3. Very similar spatial patterns
208 to those already found with NCEP/NCAR are obtained. In particular, in ERA-Interim an
209 enhanced heat loss that is slightly smaller in magnitude but still more than three standard
210 deviations from the long-term mean is found in the same eastern SPG location, as with
211 NCEP/NCAR. A similar pattern is also obtained in the subtropics although the significance

level of the anomalies is enhanced in the ERA-Interim analysis (contours in the figure indicate two subtropical regions where the anomalies are greater than two standard deviations from the long-term mean). Note that W14 net heat flux data is not yet available from OAFlux but turbulent heat flux data is available and we consider that below. The NCEP/NCAR patterns of turbulent flux anomalies are compared with corresponding fields from ERA-Interim and OAFlux in Fig 4. Again the flux anomalies are very similar in terms of magnitude and spatial distribution. The only substantive difference from NCEP/NCAR is that the subtropical anomalies are more significant (greater than two standard deviations from the long-term mean) in ERA-Interim and OAFlux.

The sensible and latent heat fluxes have similar patterns in the subtropics and thus contribute to the decreased (increased) net oceanic heat loss in the western (eastern) parts of the basin. The increased latent heat flux in the subpolar region and the decreased latent heat flux in the western subtropics imply that the source of increased water vapour in the atmosphere during W14 was primarily from the subpolar region. Previously, it has been hypothesized that the long-term warming of the sub-tropical Atlantic Ocean would have provided the source of extra atmospheric moisture feeding UK bound storms (Slingo et al. 2014). While this is a valid generalized response to long-term warming of the subtropical Atlantic, we note that in W14 the source of this additional moisture was not an increase in ocean evaporation from the subtropical Atlantic. More specifically, Fig. 5 shows the total evaporation from the Atlantic Ocean as a function of latitude band for the 35-year mean and also for W14. Although, in the mean there is more evaporation in the subtropics than at subpolar latitudes, in W14, evaporation was reduced in the subtropics and enhanced in the subpolar region. This conclusion is supported by a corresponding calculation carried out with ERA-Interim and OAFlux (see Fig. 5b and c). To further understand the subpolar-subtropical

difference in W14 flux anomalies, we examine next the surface variables that drive the fluxes.

The turbulent fluxes are proportional to the difference between T_s and T_a in the case of sensible heat flux, and the difference between q_s and q_a in the case of latent heat flux. The anomalous W14 fields for T_a, T_s and ΔT ($=T_s-T_a$) are plotted in Fig. 6. The T_a field shows a broad negative anomaly approaching -2 ºC over much of the SPG. There is also a negative anomaly in T_s but this is weaker (-1 ºC) and more spatially confined. Consequently, ΔT is larger than the mean (as the cold T_a anomaly is only partially offset by that in T_s) by of order 1ºC over the enhanced flux region of the SPG (Fig. 6c). Between 40ºW and 20ºW, this is greater than two standard deviations difference from the long-term mean. In the western subtropics, the anomalously weak sensible heat loss is associated with warmer than normal T_a, partly offset by warmer than normal T_s.

The subpolar latent heat flux is likewise enhanced, due to similar surface conditions (Fig. 7). An enhanced difference between q_s and q_a of order 1 g kg^{-1} is particularly evident in the eastern SPG. This is associated with anomalously dry air over the 40-55ºN band, partly offset by lower than normal values of q_s (due to the anomalously cool sea surface). In the western subtropics, decreased latent heat loss is associated with increased q_a, offset by higher than normal values of q_s.

Summarizing the analysis of surface net heat flux, the strongest, most significant anomalies of W14 occurred over the SPG, and in particular to the east of 40ºW. They were caused by colder and drier surface air exiting the North American continent and Nordic Seas, and enhanced winds associated with the passage of a series of particularly strong mid-latitude storms. These factors acted together to produce greatly enhanced sensible and latent heat fluxes. The enhanced turbulent fluxes were opposed to some extent by cooler T_s (and the

corresponding lower values of q_s). The implication is that the air-sea fluxes were largely forced by atmospheric variability. However, the caveat to this is that compared to recent decades, SSTs were relatively high in the subpolar gyre at the onset of winter 2013/14, and thus the region was somewhat preconditioned for enhanced wintertime heat loss.

3.1.3 Surface Freshwater Fluxes

We now turn our attention to the components of the freshwater flux and the sea surface salinity anomalies (Fig. 8). Anomalously high mid-latitude precipitation is evident in W14 concentrated on the eastern Atlantic (45-65ºN, 30ºW-0ºE) (Fig. 8a). The increase of 0.5 x 10^{-8} m/s (equivalent to just over 13 mm $month^{-1}$) just to the west of Ireland was over three standard deviations greater than the long-term average. As regards to the surface freshwater flux, the precipitation anomaly is largely cancelled out by the enhanced evaporation (discussed previously in the form of the latent heat flux) that occurred in the subpolar region stretching from the Labrador Sea to the Bay of Biscay (Fig. 8b). However, there remains a small region (55-65ºN, 20-10ºW) with significantly enhanced net freshwater input into the ocean (see Fig 1b). The March 2014 sea surface salinity (SSS) anomaly field in the subpolar gyre does not show a clear correspondence with the P-E field and has features greater than one standard deviation from the long-term mean. This suggests that the ocean circulation and mixed layer processes have played a significant role in quickly redistributing (vertically and horizontally) W14 surface freshwater flux anomalies in the subpolar gyre.

By contrast there is one region in the central subtropical Atlantic where the surface freshwater fluxes appear to have left an imprint on the surface salinity field. Near 40ºW and 30ºN, the March salinity was more than two standard deviations greater than the mean. This change in salinity is consistent with the increased net evaporation due to both decreased

precipitation and the increased evaporation mentioned previously in the context of the latent heat flux.

Again, similar results are obtained for the W14 precipitation and evaporation anomalies with ERA-Interim (note precipitation fields are not available from OAFlux but the evaporation anomalies, not shown, are similar to both NCEP/NCAR and ERA-Interim). The ERA-Interim W14 precipitation and evaporation anomaly fields are shown in Fig. 9. In each case, the anomaly fields are very similar in terms of magnitude and spatial distribution to those already presented for NCEP/NCAR. Thus, our freshwater flux conclusions remain the same when a different reanalysis product is considered.

3.2 Short-term Changes and Impacts in the Ocean-Atmosphere System

We now examine some of the short-term changes and impacts, in the atmosphere and ocean, associated with the anomalous air-sea fluxes, with particular emphases on atmospheric moisture transport, ocean circulation and ocean heat storage.

3.2.1 Atmospheric Moisture Transport Pathways

Extensive flooding in mid-latitude regions, such as that which occurred in the British Isles during W14, has been associated with anomalous patterns of moisture transport in the lower troposphere (e.g. Lavers et al 2012). We therefore examine the atmospheric moisture transport (also known as the "atmospheric river") in W14 compared to climatology (Fig. 10 a,b). We also examine the transport associated with mean winds and W14 humidity (Fig. 10c), and with W14 winds and mean humidity (Fig. 10d), to separate the influence of anomalous winds and anomalous humidity. The mean path of maximum water vapour transport is from 75ºW 35ºN in the subtropics, north-eastward to 30ºW 45ºN. In W14, the path was strengthened throughout and extended at its northern end. This northern extension

curves to the north north-east, reaching the far-eastern SPG (15º W, 45ºN). Considering the decomposed fields (Fig. 10c,d), we note that anomalous humidity (Fig. 10c) increases (slightly decreases) moisture transport in the subtropics (eastern subpolar region). However, north of 40ºN most of the enhanced moisture transport, in particular the extension to the north north-east, was associated with the stronger winds (Fig. 10d) rather than higher moisture content.

3.2.2 Ocean circulation

Using the EN4 dataset we have calculated the mean and anomalous 2014 March potential temperature for the latitude-depth section along the 30ºW meridian (Fig. 11). These potential temperature data have been used along with corresponding salinity data to calculate the mean and anomalous baroclinic geostrophic velocity along the same section. The strong meridional temperature gradient near 45ºN denotes the location of the North Atlantic Current (NAC). While the NAC transports warm saline water eventually northward to the Nordic Seas, it has a large zonal component at this location. With regard to March 2014, we note that north of 40ºN significant surface cooling (as much as 1-2º C) penetrates to 500 m. In the absence of any significant cooling to the south of 40ºN and relatively smaller changes in salinity, the effect of the northern cooling is to strengthen the meridional density gradient and consequently increase the zonal geostrophic flow, by up to 5 cm s^{-1} (Fig. 11b). The cooling on the poleward flank of the NAC also causes the maximum temperature gradient and core of the NAC to shift southwards by around 2º (comparing black and green lines in Fig. 11b).

3.2.3 Ocean heat storage

The impact of the anomalous heat loss on SPG heat content is now considered. Fig. 12a shows a January 2002 - June 2014 time series of anomalous heat content for the top 2000m of the subpolar gyre region (from 41ºN to 65ºN, across the whole basin). The time series is derived from EN4 data and has the annual cycle removed. During the first three months of 2014, ocean heat content declined markedly from an anomalously high state to the lowest value since January 2004. The loss of heat was due to either anomalous ocean heat transport divergence, the anomalous surface heat flux as previously described, or a combination of the two. Unfortunately, there are no ocean observations that measure these two processes with sufficient accuracy to specifically diagnose their relative contributions to temporal changes in heat content. However, surface fluxes from atmospheric reanalyses do provide strong evidence that the recent reduction in heat content was primarily due to anomalous air-sea heat exchange. After removing the annual cycle, between November 2013 and April 2014 there was 6.7 x 10^{21} J reduction in the SPG ocean heat content. According to the de-seasoned NCEP/NCAR net heat flux fields, this coincided with an increase in ocean heat loss from surface fluxes of 5.6 x 10^{21} J from climatology for this time of year. The attribution of this large change in SPG heat content to anomalous air-sea fluxes is atypical, further indicating the unusual nature of winter 2013-14. Numerous studies using hindcasts from high resolution ocean models have indicated that it appears to be more typical for large changes in the SPG heat content, such as the mid 1990s warming, to be driven by variability in the mid-latitude meridional ocean heat transport (Marsh et al. 2008; Grist et al. 2010).

3.3 Long-term Impacts on the Regional Climate System.

We finally consider the longer-term impacts of anomalous W14 forcing on the ocean, and possibly the atmosphere, hence the regional climate system. First, we quantify the

anomalous wintertime formation of Subpolar Mode Water (SPMW), and then investigate the regional reverberation of this water mass formation through trajectory analyses.

3.3.1 Formation of SPMW

Surface-forced water mass transformation and formation rates in the SPG, calculated as outlined in Section 2 (following Speer and Tziperman, 1992), are shown in Fig. 13. In the density range $27.1 < \sigma_0 < 27.4$ kg m^{-3}, transformation rates for W14 exceed the standard deviation about long-term means averaged over 1979-2013, peaking around 20 Sv at σ_0 = 27.3 kg m^{-3}, compared to a long-term mean of ~12.5 Sv (Fig. 13a). The corresponding formation rates (derivatives of transformation rates with respect to density, computed at "mid-point" densities) reveal anomalous water mass formation of ~7 Sv centred on σ_0 = 27.35 kg m^{-3}, substantially above the long-term mean of ~2 Sv (Fig. 13b). The similarly large negative anomalies at σ_0 = 26.85 and 27.05 kg m^{-3} are consistent with stronger "consumption" of water in these lighter density classes, balancing the stronger formation of SPMW. To put SPMW formation of W14 in more historical context, in Fig. 13c we show annual formation rates in two density classes representative of SPMW – centered on σ_0 = 27.35 and 27.45 kg m^{-3}, close to core values in the region (see de Boisséson et al. 2012, and references therein) – and the mean of these two classes. It is evident that the combined formation rates for these two densities reached the highest value since 1979, in W14.

Identifying enhanced surface formation in the density range $27.3 < \sigma_0 < 27.5$ kg m^{-3}, in Fig. 14 we map the thickness of the corresponding layer in the EN4 data, for March (the end of winter) to July, averaged over 1979-2013, for 2014, and the "2014 minus 1979-2013 mean" anomalies. The mean thickness distributions reveal maximum thickness in the northeast Atlantic, with thickness gradually eroded over March-July. In 2014, the area where

thicknesses exceeded 400 m spread notably to the south and west. This is evident in the anomaly fields, with the most extensive thickness anomalies (> 200 m) evident in April, but thickness anomalies > 100 m persisting along the southern flank of the SPG through July.

3.3.2 Transport, dispersal and transformation of anomalous SPMW

To investigate the likely fate of the SPMW thickness anomaly over seasonal to interannual timescales, we make a first-order assumption that this mode water will move passively with the general circulation and disperse as in previous years. To illustrate the transport of SPMW, horizontal dispersal by eddies and diapycnal transformation through mixing and subsequent air-sea interaction, we generate ensembles of particle trajectories using the property and velocity fields from two eddy-resolving ocean model hindcasts, ORCA12 and OFES, calculated with methods that have been developed for particle-tracking in each hindcast (ARIANE and CMS respectively). Using 5-daily ORCA12 velocity and tracer fields, ARIANE particles are released five times, 5 days apart, through April of 1988-2006, on a 1° x 1° grid at 77 locations where the April 2014 SPMW layer thickness anomaly exceeded 200 m, every ~100 m from 100-500 m. The 3D location and property for each particle is saved to file every 5 days, up to day 540 (109 times). A similar strategy is adopted for OFES and CMS, where velocity fields are available every three days. We then sample the particles after 180, 360 and 540 days, to obtain maps of particle density (as a fraction of the original number of particles released), illustrating the transport, lateral mixing and diapycnal erosion of the representative SPMW anomaly. The results are summarized in Figure 15. Overall, the two methods and datasets provide the same indication of drift to the northeast, with a limited number of particles reaching the East Greenland Current and the Norwegian Coastal Current by day 180, and substantial spreading both initially (by day 180) and subsequently (over days 180-540). By day 540, there is considerable divergence of particles

406 between destinations in the SPG and the Norwegian Sea, with overall stronger dispersion and
407 divergence, but less erosion via further transformation, in OFES.
408
409 To further explore the likely re-emergence of anomalously cold SPMW in the subsequent
410 winter of 2014/15, we analyse OFES/CMS trajectories to see where and when particles are
411 re-entrained into the mixed layer. For each particle, we find out where and when it first
412 reached into the mixed layer (as defined by the mixed layer depth field from the OFES
413 simulation). To count only re-emergence in the subsequent winter, we do not consider
414 crossings into the mixed layer during the first 165 days (from April).
415
416 Fig. 16 shows when (Fig. 16a,b) and where (Fig. 16c) particles cross into the mixed layer.
417 Most re-entrainment into the mixed layer happens between the UK and Iceland, in the early
418 winter after the year of release (so 7 to 10 months after the month of April for which we
419 started the particle trajectories), i.e., between November and January; 77% of all particles
420 actually re-emerge in the first winter season after release, according to this analysis. Fig 16c
421 provides a projection of where the component of any autumn 2014 SST anomaly associated
422 with anomalous W14 SPMW may occur. However, considering the strength and depth of
423 W14 ocean cooling, reemergence may not be restricted to SPMW or this specific area.
424 Furthermore other air-sea interactions of winter 2014-2015 may lead to additional negative
425 (and positive) SST anomalies. We have examined whether there are any early signs of re-
426 emergence using NCEP/NCAR SST fields for late summer and early winter 2014. Figure 16d
427 shows the difference in SSTA for 1-10 November 2014 relative to the earlier 10 day period
428 September 20-30 2014 (chosen because it samples conditions at the end of summer when
429 significant re-emergence is not yet expected to have occurred). This figure indicates the
430 development of a cool SST feature over much of the region. This is consistent with the

proposal that some of the water cooled in W14 will undergo reemergence the following autumn/winter and that part of the re-emergent signal is associated with the anomalous formation of SPMW.

4. Summary

We utilized NCEP/NCAR and ERA-Interim reanalyses and the OAFlux data set to examine the extreme North Atlantic winter of 2013-14, with a particular focus on the role of air-sea interaction and subsequent impacts on the ocean. The strongest anomalies in the net surface heat flux were located in the SPG and these were notably enhanced in the eastern half of the basin. This anomaly was comprised primarily of exceptional latent and sensible heat loss in the northeast Atlantic, associated with anomalously strong north-westerly winds, bringing exceptionally cold and dry air across the northeast Atlantic.

The anomalous surface heat loss left an immediate imprint on the ocean in a number of ways. First the cooling to depth on the poleward flank of the NAC, led to a strengthening of the meridional temperature (and density) gradient. This had the effect of increasing the maximum zonal geostrophic flow associated with the NAC. Additionally there was a southward shift of this core. Second, the heat content of the upper 2000 m reduced markedly to the lowest level since January 2004. Previous modelling studies (e.g. Marsh et al. 2008; Grist et al. 2010) indicate that the attribution of such a significant change in SPG heat content to air-sea fluxes is atypical, illustrating the strength of the heat flux anomalies in W14.

The longer-term legacy of winter 2013/14 is an anomalously cold and dense volume of Subpolar Mode Water - one of the precursors of North Atlantic Deep Water (e.g., Langehaug, et al. 2012, and references therein) and thus an important component of the Atlantic Meridional Overturning Circulation (AMOC). The subpolar gyre has previously been linked to decadal-timescale changes further to the north (Hátún et al., 2005). Here, we

456 have focused on a possible shorter-term response. Using particle trajectory analysis, we
457 investigated the likely dispersal of this SPMW on timescales up to 18 months, to encompass
458 seasonal-interannual impacts on the regional climate system.

459 Re-emergence of wintertime SSTA patterns in subsequent winters is ubiquitous
460 throughout much of the extratropical World Ocean (Hanawa and Sugimoto, 2004). The 2013-
461 14 winter SSTAs are similar in magnitude to previous re-emergence episodes in the wider
462 North Atlantic (e.g. winters 2009-10 and 2010-11, Taws et al., 2011), but are more clearly
463 subject to dynamical influences (the North Atlantic Current) that will lead to a degree of
464 "remote re-emergence" (Sugimoto and Hanawa, 2005). Consequently, we expect downstream
465 re-emergence of the anomalously cold W14 SPMW in subsequent winters. Coherent drift and
466 limited dispersal of the majority of SPMW "particles" suggest to us that statistically
467 significant negative SST anomalies may indeed re-emerge during winter 2014/15 between the
468 British Isles and Iceland, to the northeast of the initial formation site. This prediction is
469 supported by preliminary analysis of re-emergent OFES/CMS particles, with further ancillary
470 evidence in the evolving SSTA field for early November 2014 (Fig. 16).

471 To conclude, the winter of 2013-14 was exceptional as regards to the turbulent heat
472 flux anomalies experienced in the North Atlantic eastern subpolar gyre. These left an imprint
473 on the ocean both in the sea surface temperature and the formation rate of SPMW that may be
474 expected to have near-term consequences through re-emergent surface temperature signals.
475 Possible longer-term consequences are a slow baroclinic adjustment of the subpolar gyre to
476 perturbed density gradients and/or a response of the AMOC to "upstream" changes in SPMW
477 formation.
478

Acknowledgements

RM acknowledges the support of a Faculty of Science Research Fellowship awarded by the University of New South Wales, and the support of a 2013 Research Bursary awarded by the Scottish Association for Marine Science. EVS was supported by the Australian Research Council via grant DE130101336. ZJ is supported by a studentship from the Graduate School of the National Oceanography Centre Southampton.

References

Ballinger TM, Allen MJ, Rohli RV (2014) Spatiotemporal analysis of the January Northern Hemisphere circumpolar vortex over the contiguous United States. Geophys Res Lett 41: 3602-3608. doi:10.1002/2014GL060285

Barnier B, Madec G, Penduff T, Molines J-M, Treguier A-M, Le Sommer J, Beckmann A, Biastoch A, Böning C, Dengg J, Derval C, Durand E, Gulev S, Remy E, Talandier C, Theetten S, Maltrud M, McClean J, De Cuevas B (2009) Impact of partial steps and momentum advection schemes in a global ocean circulation model at eddy permitting resolution. Ocean Dyn 56: 543-567. doi:10.1007/s10236-006-0082-1

Blanke B, Raynaud S (1997) Kinematics of the Pacific Equatorial Undercurrent: a Eulerian and Lagrangian approach from GCM results. J Phys Oceanogr 27: 1038-1053

de Boisséson E, Thierry V, Mercier H, Caniaux G (2012) Origin, formation and variability of the subpolar mode water observed over the Reykjanes Ridge. J Geophys Res (Oceans) 117: C12005, doi:10.1029/2011JC007519

Dee DP, et al. (2011) The ERA-Interim reanalysis: Configuration and performance of the data assimilation system. Quart J Roy Meteor Soc, 137, 553–597. doi:10.1002/qj.828

DRAKKAR Group (2007) Eddy-permitting Ocean Circulation Hindcasts of past decades. CLIVAR Exchanges, 42, 12(3), 8-10.

Duchez A, Frajka-Williams E, Castro N, Hirschi J, Coward A (2014) Seasonal to interannual variability in density around the Canary Islands and their influence on the Atlantic meridional overturning circulation at 26°N. J Geophys Res Oceans 119: 1843–1860. doi:10.1002/2013JC009416

Good, SA, Martin MJ, Rayner NA (2013) EN4: quality controlled ocean temperature and salinity profiles and monthly objective analyses with uncertainty estimates. J. Geophys. Res., 118, 6704-6716, doi:10.1002/2013JC009067

Grist JP, Josey SA, Boehme L, Meredith MP, Laidre KL, Heide- Jørgensen MP, Kovacs KM, Lydersen C, Davidson FJM, Stenson GB, Hammil MO, Marsh R, Coward AC (2014) Seasonal variability of the warm Atlantic Water layer in the vicinity of the Greenland shelf break. Geophys Res Lett 41: 8530–8537, doi: 10.1002/2014GL062051

Grist JP, Josey, SA, Marsh R, Good SA, Coward AC, de Cuevas BA, Alderson SG, New AL, Madec G (2010) The roles of surface heat flux and ocean heat transport convergence in determining Atlantic Ocean temperature variability. Ocean Dyn 60: 771–790. doi: 10.1007/s10236-010-0292-4

529

530 Grist JP, Marsh R, Josey SA (2009) On the relationship between the North Atlantic
531 meridional overturning circulation and the surface-forced overturning stream function. J
532 Clim 22: 4989-5002. doi:10.1175/2009JCLI2574.1

533

534 Hanawa K, Sugimoto S (2004) Re-emergence areas of winter sea surface temperature
535 anomalies in the world's oceans. Geophys. Res. Lett 31: doi:10.1029/2004GL019904

536

537 Hátún H, Sandø AB, Drange H, Hansen B, Valdimarsson H (2005) Influence of the Atlantic
538 Subpolar Gyre on the Thermohaline Circulation. Science 309: 1841-1844, doi:
539 10.1126/science.1114777

540

541 Hecht, MW, Smith RD (2013) Toward a physical understanding of the North Atlantic: a
542 review of model studies in an eddying regime. Geophys Monogr Ser 177: 213–239

543

544 Hobbs WR, Willis JK (2012) Midlatitude North Atlantic heat transport: A time series based
545 on satellite and drifter data. J Geophys Res 117: C01008. doi:10.1029/2011JC007039

546

547 Huntingford C, Marsh T, Scaife AA, Kendon EJ, Hannaford J, Kay AL, Lockwood M,
548 Prudhomme, Reynard NS, Parry S, Lowe JA, Screen JA, Ward HC, Roberts M, Stott PA,
549 Bell VA, Bailey M, Jenkins A, Legg T, Otto FEL, Massey MN, Schaller N, Slingo J, Allen
550 MR (2014) Potential influences on the United Kingdom's floods of winter 2013/14. Nature
551 Climate Change 4: 769-777. doi:10.1038/nclimate2314.

552

553 Josey SA, Gulev S, Yu L, (2013) Exchanges through the ocean surface, in *Siedler, G.,*
554 *Griffies, S., Gould, J. and Church, J. (Eds.): Ocean Circulation and Climate 2nd Ed. A 21st*
555 *century perspective,* Academic Press, International Geophysics Series, Volume 103, p. 115-
556 140.
557
558 Langehaug HR, Rhines PB, Eldevik T, Mignot J, Lohmann K (2012) Water-mass
559 transformation and the North Atlantic Current in three multi-century climate model
560 simulations. J Geophys Res: doi:10.1029/2012JC00802
561
562 Lavers DA, Villarini G, Allan RP, Wood EF, Wade AJ (2012) The detection of atmospheric
563 rivers in atmospheric reanalysis and their links to British winter floods and the large-scale
564 climatic circulation. J Geophys Res 117: D20106. doi:10.1029/2012JD018027
565
566 Madec, G (2008) NEMO Ocean Engine, Note du pôle modélisation 27, Institut Pierre-Simon
567 Laplace (IPSL).
568
569 Marsh R (2000) Recent variability of the North Atlantic thermohaline circulation inferred
570 from surface heat and freshwater fluxes. J Clim 13 : 3239-3260
571
572 Marsh R, Josey SA, de Cuevas BA, Redbourn LJ, Quartly, QD (2008) Mechanisms for recent
573 warming of the North Atlantic: insights gained with an eddy-permitting model. J Geophys
574 Res 113:C04031. doi:10.1029/2007JC004096
575
576 Masumoto Y, Sasaki H, Kagimoto T, Komori N, Ishida A, Sasai Y, Miyama T, Motoi T,
577 Mitsudera H, Takahashi K, Sakuma H, Yamagata T (2004) A fifty-year eddy-resolving

simulation of the world ocean: Preliminary outcomes of OFES (OGCM for the Earth simulator). J. Earth Simul 1: 35–56

Mathews T, Murphy C, Wilby RL, Harrigen S (2014) Stormiest winter on record for Ireland and UK. Nature Climate Change 4: 738-740. doi:10.1038/nclimate2336

Palmer T (2014) Record-breaking winters and global climate change. Science 344: 803-804. doi:101126/science.1255147

Paris, CB, Helgers J, Van Sebille E, Srinivasan A (2013) Connectivity modeling system: A probabilistic modeling tool for the multi-scale tracking of biotic and abiotic variability in the ocean. Environ. Modell. Software 42: 47–54, doi:10.1016/j.envsoft.2012.12.006

Screen JA, Deser C, Sun L (2015) Reduced risk of North American cold extremes due to continued Arctic Sea-Ice Loss. Bull Amer Meteor Soc (Early on line Release). doi: http://dx.doi.org/10.1175/BAMS-D-14-00185.1

Slingo, J, Belcher S, Scaife A, McCarthy, M, Saulter A, McBeath K, Jenkins A, Huntingford C, Marsh T, Hannaford J, Parry S (2014) The Recent Storms and Floods in the UK. Exeter, UK Met Office, 27pp. [http://nora.nerc.ac.uk/505192/]

Speer K, Tziperman E (1992) Rates of water mass formation in the North Atlantic Ocean J Phys Oceanogr 22: 93-104

Sugimoto S, Hanawa K (2005) Remote re-emergence areas of winter sea surface temperature

603 anomalies in the Norty Pacific. Geophys Res Lett., 32: doi:10.1029/2004GL021410
604
605 Taws SL, Marsh R, Wells NC, Hirschi J (2011) Re-emerging ocean temperature anomalies in
606 late-2010 associated with a repeat negative NAO. Geophys Res Lett 38(20): L20601.
607 (doi:10.1029/2011GL048978).
608 van Oldenborgh, GJ, Haarsma R, De Vries H, Allen MR (2015) Cold Extremes in North
609 America vs. Mild Weather in Europe: The Winter of 2013–14 in the Context of a Warming
610 World. Bull Amer Meteor Soc 96: 707–714. doi: http://dx.doi.org/10.1175/BAMS-D-14-
611 00036.1
612
613 Walin, G (1982) On the relation between sea-surface heat flow and thermal circulation in the
614 ocean. Tellus 34: 187-195
615
616 Yu, L., and R. A. Weller (2007) Objectively Analyzed air-sea heat Fluxes for the global oce-
617 free oceans (1981–2005). Bull. Ameri. Meteor. Soc., 88, 527–539.

Figures

Fig. 1 Anomalous NCEP/NCAR air-sea fluxes over the North Atlantic for W14 relative to the 35 winters from 1979-80 to 2013-14. a) net heat flux (W m^{-2}), b) net freshwater flux (m s^{-1}) (precipitation minus evaporation) and c) momentum flux (N m^{-2}). The black contours denote anomalies that are greater than two and three standard deviations from the mean. d) anomalous W14 sea level pressure (shading, mb) and 10 m wind vectors (arrows). Positive values denote fluxes into the ocean.

Fig. 2 Anomalies in the different components of the W14 NCEP/NCAR surface net heat flux. a) Latent heat flux b) sensible heat flux; c) net shortwave radiation; d) net longwave radiation. All units are W m^{-2}. The black contours denote anomalies that are greater than two and three standard deviations from the mean. Negative values denote an increase in oceanic heat loss.

Fig. 3 a) Anomalous ERA-I net heat flux over the North Atlantic for W14 relative to the 35 winters from 1979-80 to 2013-14. The black contours denote anomalies that are greater than two and three standard deviations from the mean. b) anomalous W14 sea level pressure (shading, mb) and 10 m wind vectors (arrows).

Fig. 4 W14 Anomalies in the turbulent heat fluxes in ERA-I and OAFlux a) latent heat flux (ERA-I); b) sensible heat flux (ERA-I) ; c) latent heat flux (OAFlux) d) sensible heat flux (OAFlux). All units are W m^{-2}. The black contours denote anomalies that are greater than two and three standard deviations from the mean. Negative values denote an increase in oceanic heat loss.

641 **Fig. 5** The total winter (DFJ) evaporation (kg) in 1º latitude band over the North Atlantic
642 Ocean. The black line denotes the long-term mean and the grey line denotes W14. a) NCEP-
643 NCAR, b) ERA-I and c) OAFlux.
644 **Fig. 6** Anomalous NCEP/NCAR W14 fields for a) 2m air temperature; b) surface or skin
645 temperature and c) surface minus air temperature or ΔT. All units are ºC. The black contours
646 denote anomalies that are greater than two and three standard deviations from the mean.
647 **Fig. 7** Anomalous NCEP/NCAR W14 fields for a) 2m specific humidity; b) saturation
648 specific humidity at the surface or skin temperature and c) b) minus air a) or Δq. All units are
649 g kg^{-1}. The black contours denote anomalies that are greater than two and three standard
650 deviations from the mean.
651 **Fig. 8** Anomalous NCEP/NCAR W14 fields of a) precipitation and b) evaporation. Units are
652 m s^{-1}. c) Anomalous EN4 sea surface salinity (SSS) for W14. The black contours denote
653 anomalies that are greater than two and three standard deviations from the mean. Note
654 precipitation minus evaporation is shown in Fig. 1b).
655 **Fig. 9** Anomalous ERA-I W14 fields of a) precipitation and b) evaporation. Units are m s^{-1}.
656 The black contours denote anomalies that are greater than two and three standard deviations
657 from the mean.
658 **Fig. 10** Integrated atmospheric zonal moisture transport IVT for DJF of a) mean of winter
659 1979-80 to winter 2013-14, b) for W14. c) the IVT calculated using the mean winter winds
660 and the W14 humidity and d) calculated with W14 winds and the mean winter humidty
661 fields. Atmospheric moisture transport is vertically integrated from 1000mb to 300mb and the
662 units are kg m^{-1} s^{-1}. The relevant zonal and meridional components are shown as arrows.
663 **Fig. 11** a) Mean 2002-14 March Temperature at 30ºW as function of latitude and depth. b) as
664 a) but showing anomaly for March 2014. c) Mean 2002-14 March geostrophic velocity at
665 30ºW as function of latitude and depth. d) as c) but showing anomaly for March 2014 (red

666 denotes an increase in the westward flow). Black lines in c) and d) are the 0.2 ms^{-1} contour
667 depicting the location of the strongest eastward flow and in particular the NAC at 43º N.
668 Grey line in d) shows the same but for March 2014. The black dashed lines in b) and d)
669 denote where the anomalies are greater than two and three standard deviations from the
670 mean.
671 **Fig. 12** Time series of ocean heat content (Joules) in the North Atlantic SPG (41ºN to 65ºN)
672 from January 2002 to June 2014 derived from the EN3 data set. The annual cycle has been
673 removed.
674 **Fig. 13** Surface-forced water mass transformation and formation rates in the eastern subpolar
675 gyre: (a) transformation rates averaged over 1979-2013 (blue curves, with standard
676 deviations) and for 2014 (red curve); (b) corresponding formation rates; (c) annual formation
677 rates in two density classes representative of SPMW and the mean of the two classes. The
678 two SPMW density classes are also shown denoted by green and magenta errorbars in b).
679 **Fig. 14** Thickness (m) of the layer bound by σ_0 surfaces 27.3 and 27.5 kg m^{-3}, for March-
680 July: averaged over 1979-2013 (a, c, e, g and i) and for the "2014 minus 1979-2013 mean"
681 anomaly (b, d, f, h, and j).
682 **Fig. 15** The proportion of SPMW particles (density ranging $27.3 < \sigma_0 < 27.5$ kg m^{-3}) in 1° x
683 1° gridboxes: (a), (b) after 180 days; (c), (d) after 360 days; (e), (f) after 540 days; particle
684 distributions in (a), (c) and (e) are computed with ARIANE and ORCA12 datasets; particle
685 distributions in (b), (d) and (f) are computed with CMS and OFES datasets.
686 **Fig. 16** a) Frequency distribution of time taken for SPMW particles reach the mixed layer. b)
687 Frequency distribution of calender month in which SPMW particles reach mixed layer. c)
688 Geographic frequency distribution of locations where SPMW particles reach mixed layer
689 after. All are based on the trajectory analysis with the CMS in the OFES model. d) The
690 NCEP/NCAR SST anomaly for October 2014.

691
692

Figure 1

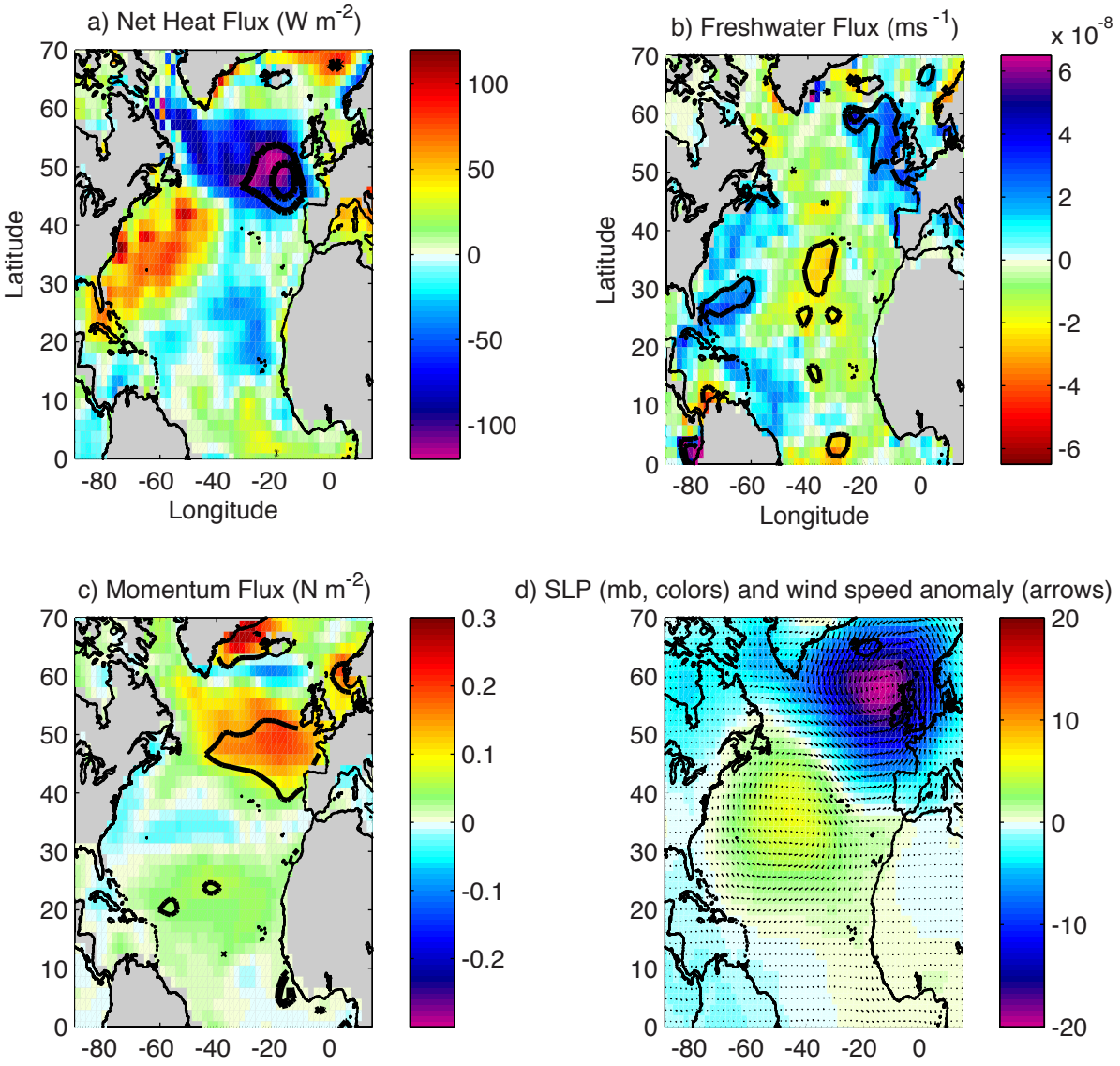

a) Net Heat Flux (W m-2)
b) Freshwater Flux (ms -1)
x 10-8
c) Momentum Flux (N m-2)
d) SLP (mb, colors) and wind speed anomaly (arrows)
Latitude
Longitude
70
60
50
40
30
20
10
0
-80 -60 -40 -20 0
100
50
0
-50
-100
6
4
2
0
-2
-4
-6
0.3
0.2
0.1
0
-0.1
-0.2
20
10
0
-10
-20

Figure 2

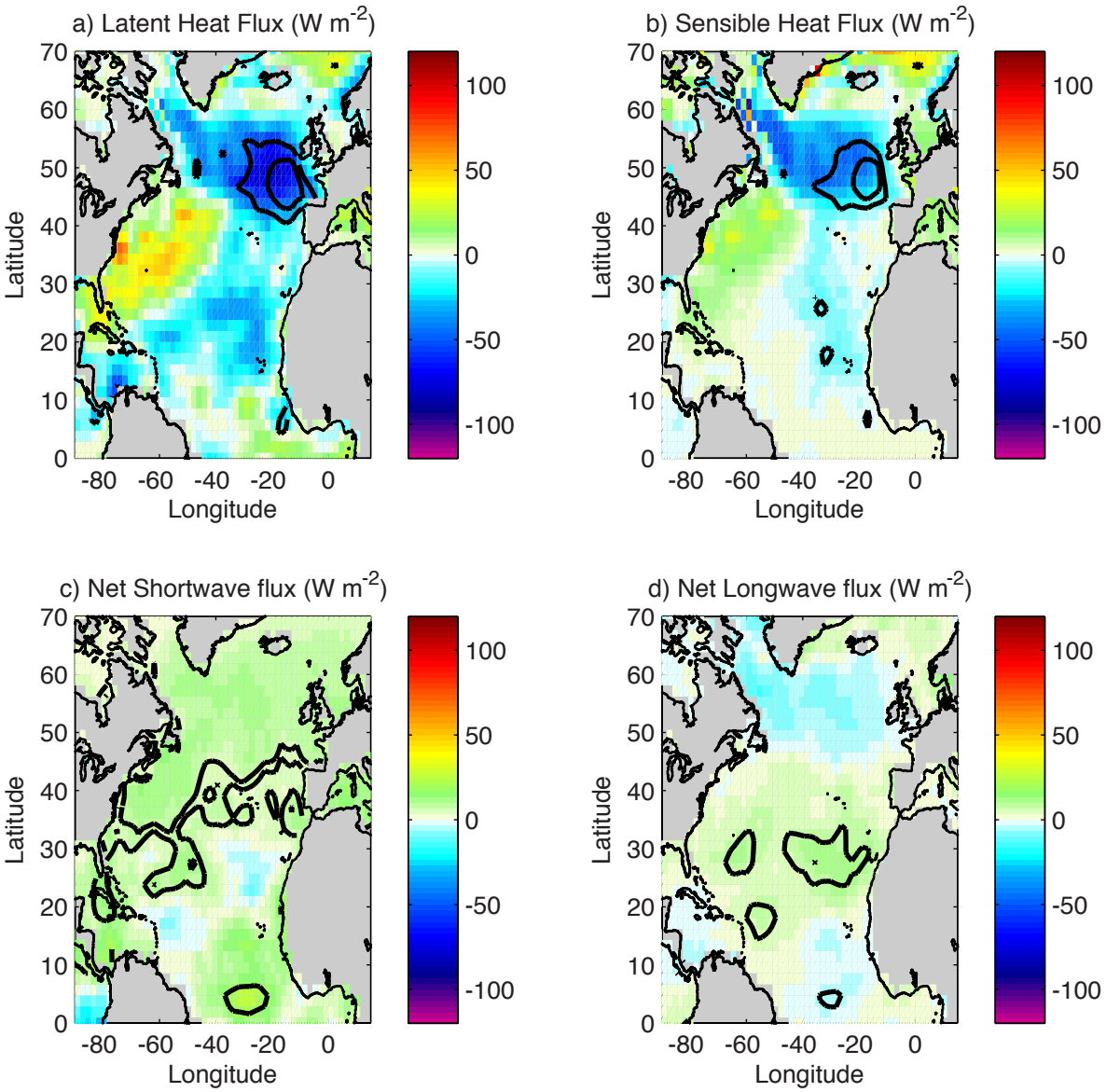

a) Latent Heat Flux (W m-2)
b) Sensible Heat Flux (W m-2)
c) Net Shortwave flux (W m-2)
d) Net Longwave flux (W m-2)
Latitude
Longitude
70
60
50
40
30
20
10
0
-80
-60
-40
-20
0
100
50
0
-50
-100

Figure 3

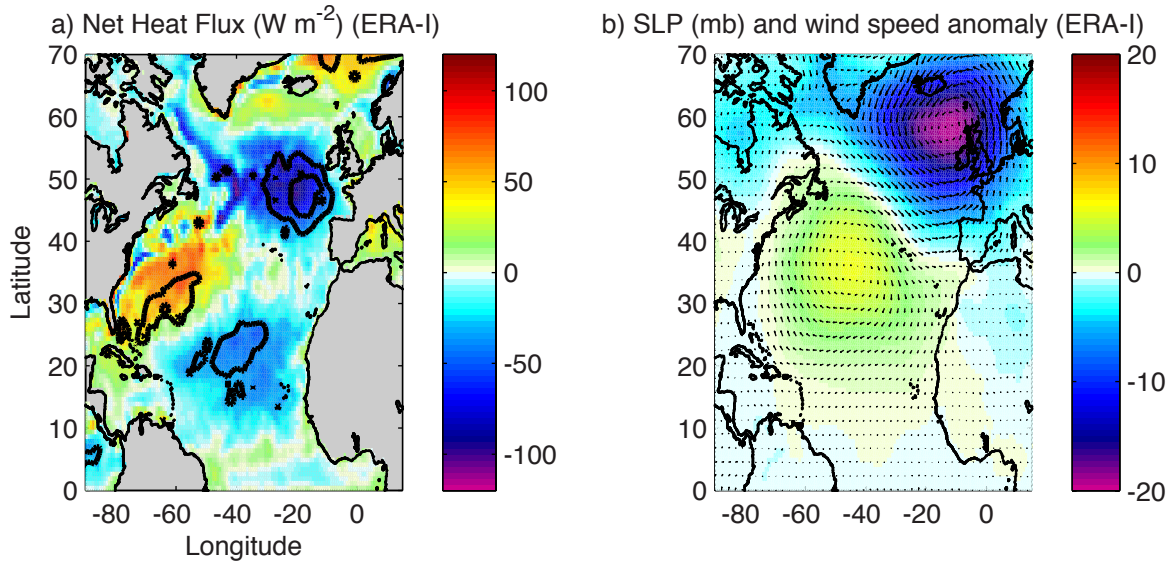

a) Net Heat Flux (W m-2) (ERA-I)
b) SLP (mb) and wind speed anomaly (ERA-I)
Latitude
Longitude
70
60
50
40
30
20
10
0
-80
-60
-40
-20
0
100
50
0
-50
-100
20
10
0
-10
-20

Figure 4

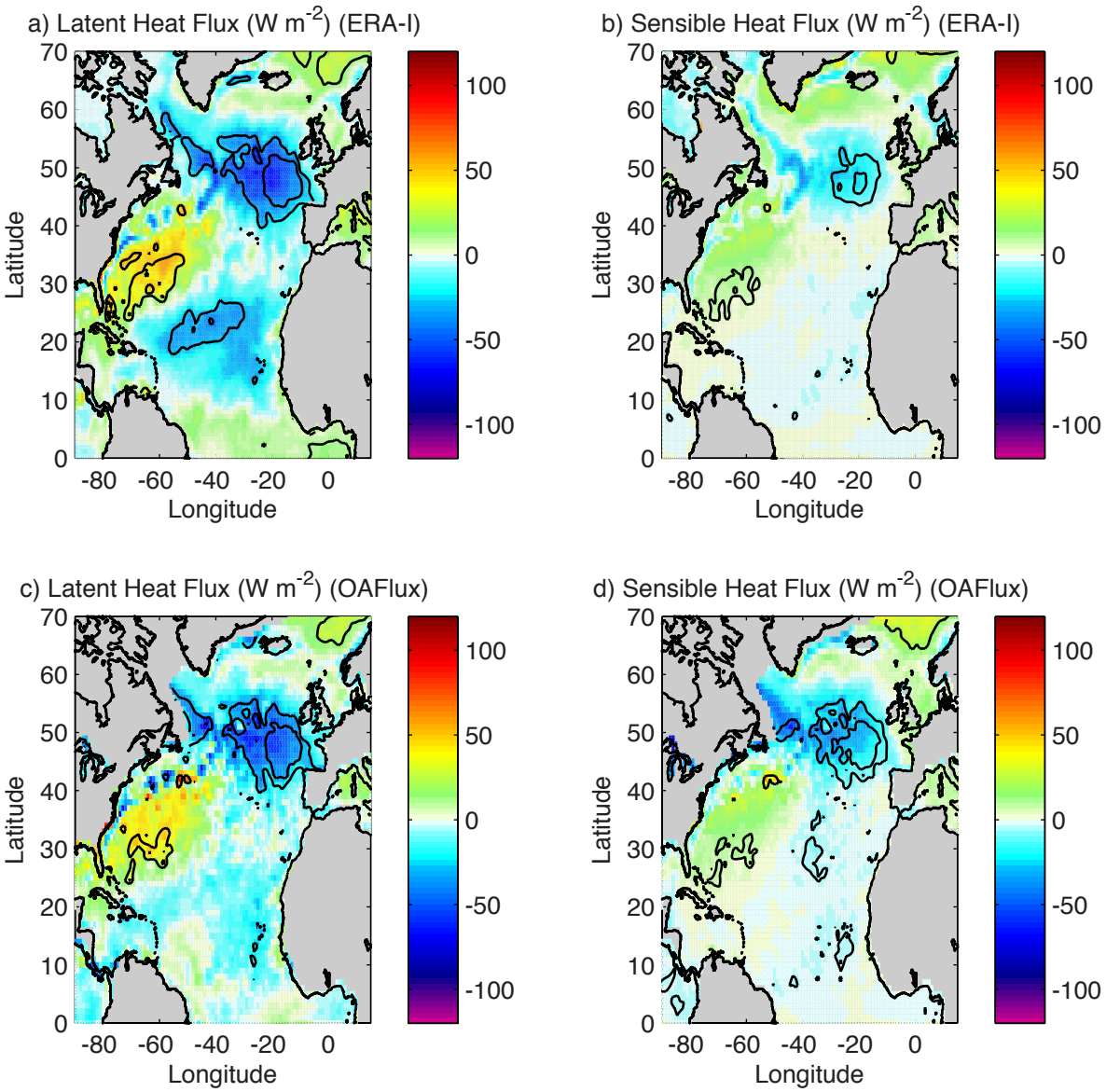

a) Latent Heat Flux (W m-2) (ERA-I)
b) Sensible Heat Flux (W m-2) (ERA-I)
c) Latent Heat Flux (W m-2) (OAFlux)
d) Sensible Heat Flux (W m-2) (OAFlux)
Latitude
Longitude
70
60
50
40
30
20
10
0
-80
-60
-40
-20
0
100
50
0
-50
-100

Figure 5

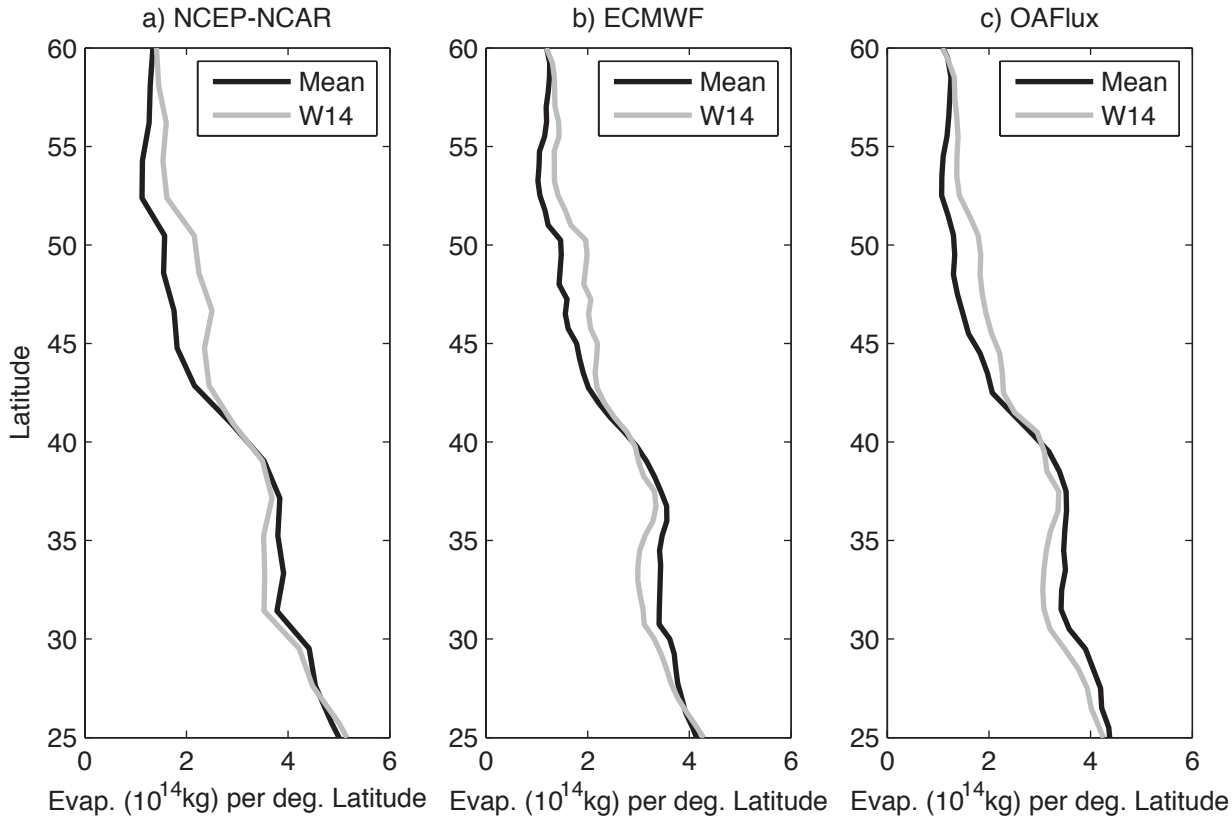

a) NCEP-NCAR
b) ECMWF
c) OAFlux
Mean
W14
Latitude
60
55
50
45
40
35
30
25
0
2
4
6
Evap. (10^{14}kg) per deg. Latitude

Figure 6

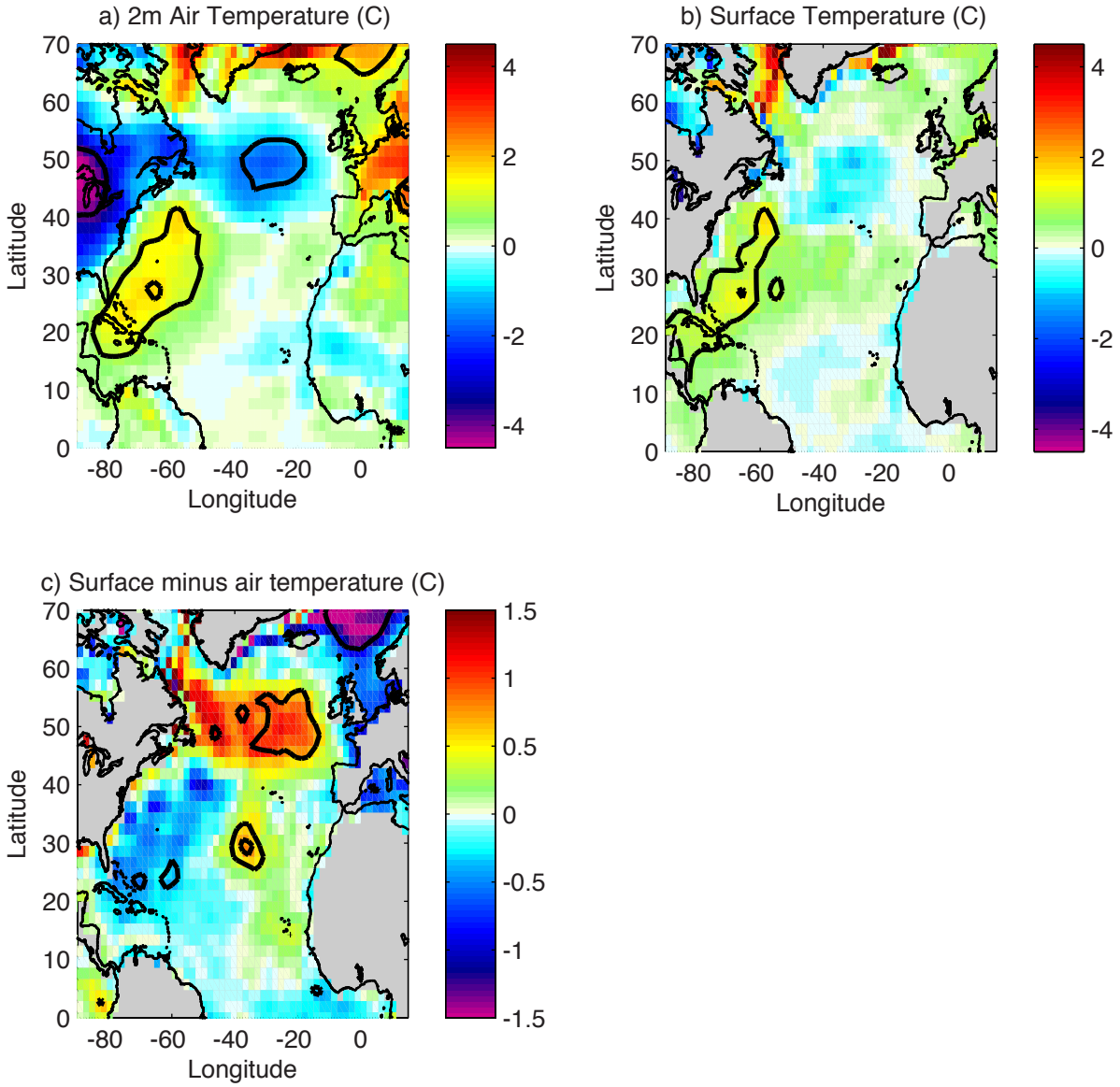

a) 2m Air Temperature (C)
b) Surface Temperature (C)
c) Surface minus air temperature (C)
Latitude
Longitude
70
60
50
40
30
20
10
0
-80
-60
-40
-20
0
4
2
0
-2
-4
1.5
1
0.5
0
-0.5
-1
-1.5

Figure 7

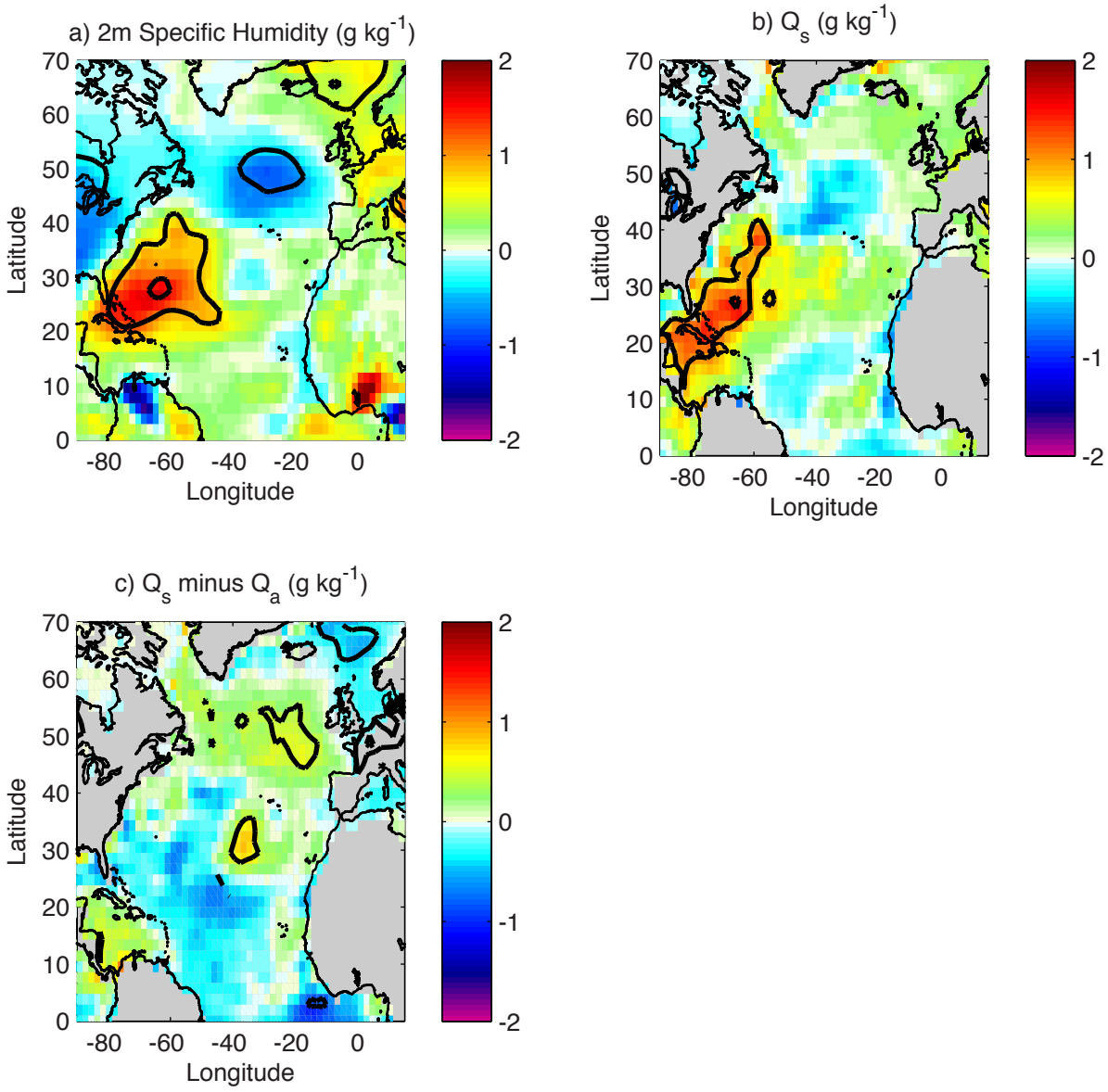

a) 2m Specific Humidity (g kg-1)
b) Qs (g kg-1)
c) Qs minus Qa (g kg-1)
Latitude
Longitude
70
60
50
40
30
20
10
0
-80
-60
-40
-20
0
2
1
0
-1
-2

Figure 8

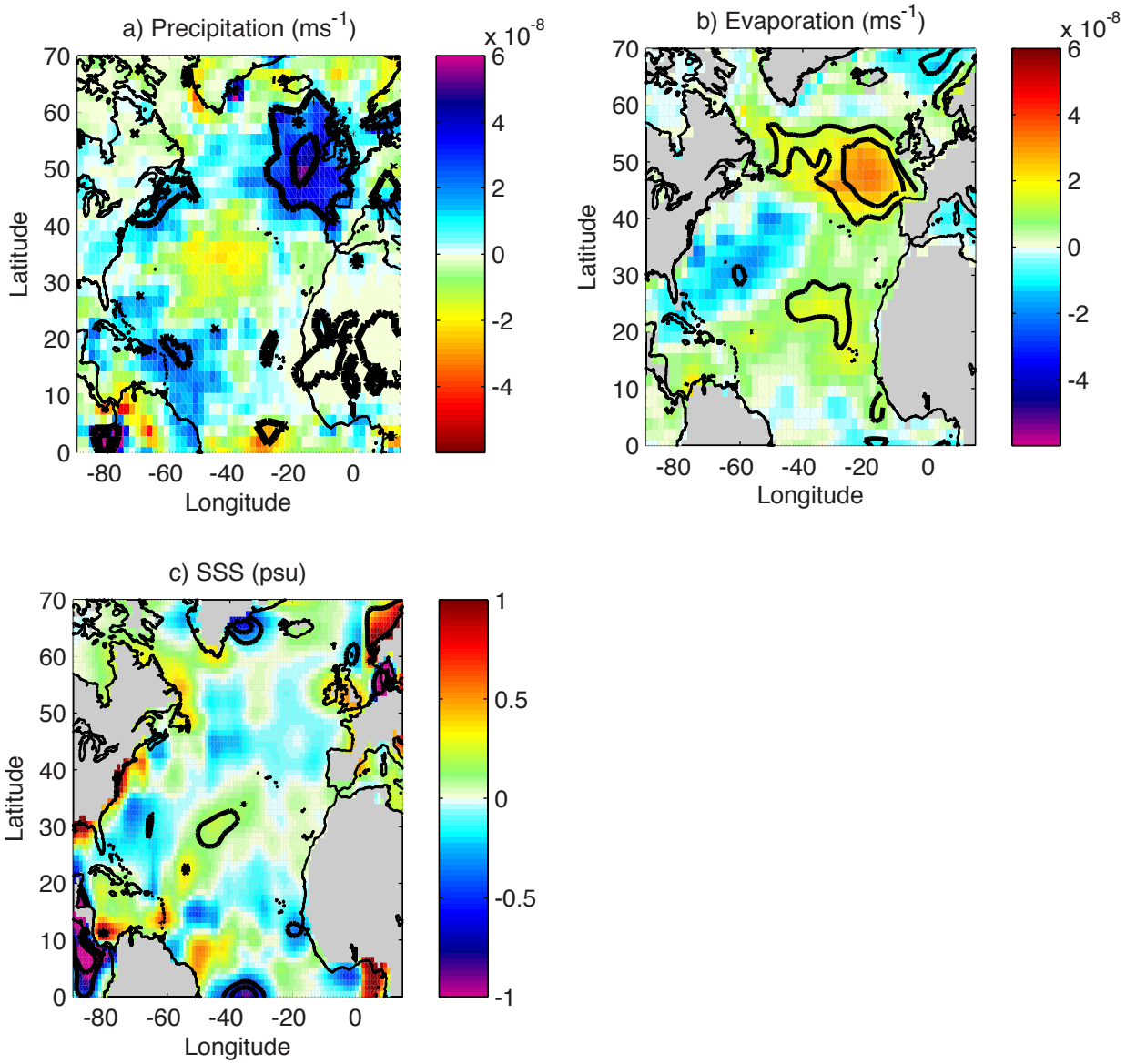

a) Precipitation (ms-1)
x 10-8
6
4
2
0
-2
-4
Latitude
70
60
50
40
30
20
10
0
-80
-60
-40
-20
0
Longitude
b) Evaporation (ms-1)
x 10-8
6
4
2
0
-2
-4
Latitude
70
60
50
40
30
20
10
0
-80
-60
-40
-20
0
Longitude
c) SSS (psu)
1
0.5
0
-0.5
-1
Latitude
70
60
50
40
30
20
10
0
-80
-60
-40
-20
0
Longitude

Figure 9

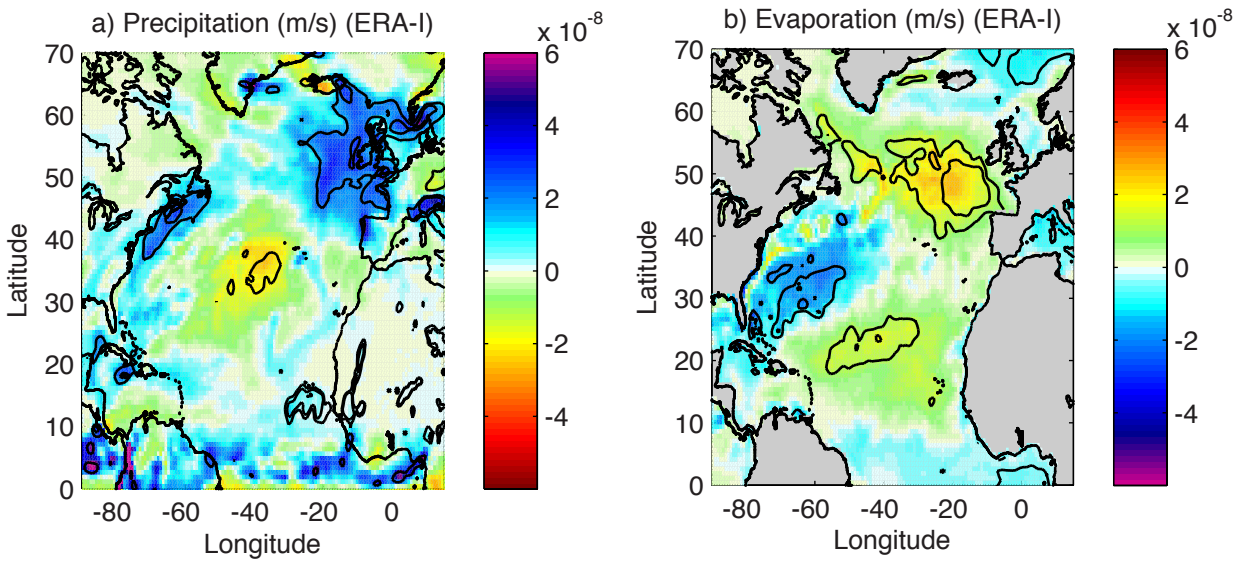

a) Precipitation (m/s) (ERA-I)
x 10^-8
6
4
2
0
-2
-4
Latitude
70
60
50
40
30
20
10
0
-80
-60
-40
-20
0
Longitude
b) Evaporation (m/s) (ERA-I)
x 10^-8
6
4
2
0
-2
-4
Latitude
70
60
50
40
30
20
10
0
-80
-60
-40
-20
0
Longitude

Figure 10

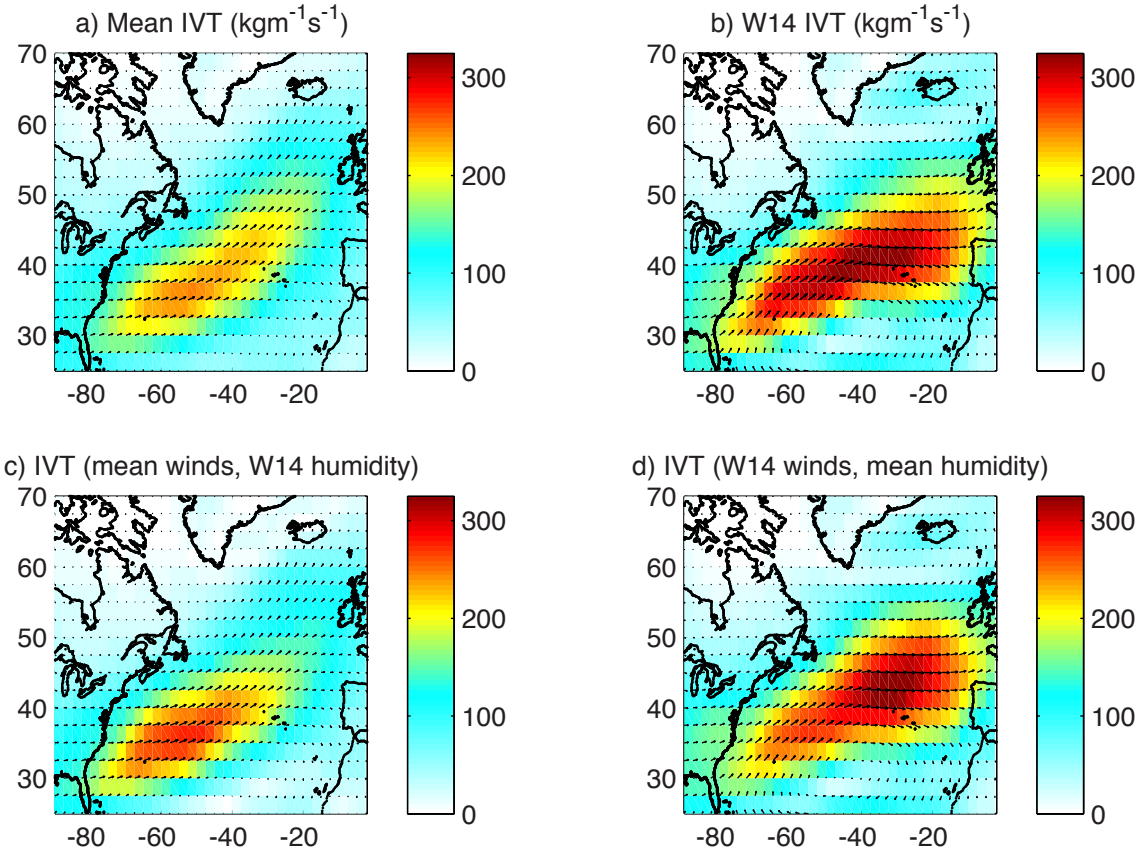

a) Mean IVT (kgm-1s-1)
b) W14 IVT (kgm-1s-1)
c) IVT (mean winds, W14 humidity)
d) IVT (W14 winds, mean humidity)
70
60
50
40
30
-80
-60
-40
-20
300
200
100
0

Figure 11

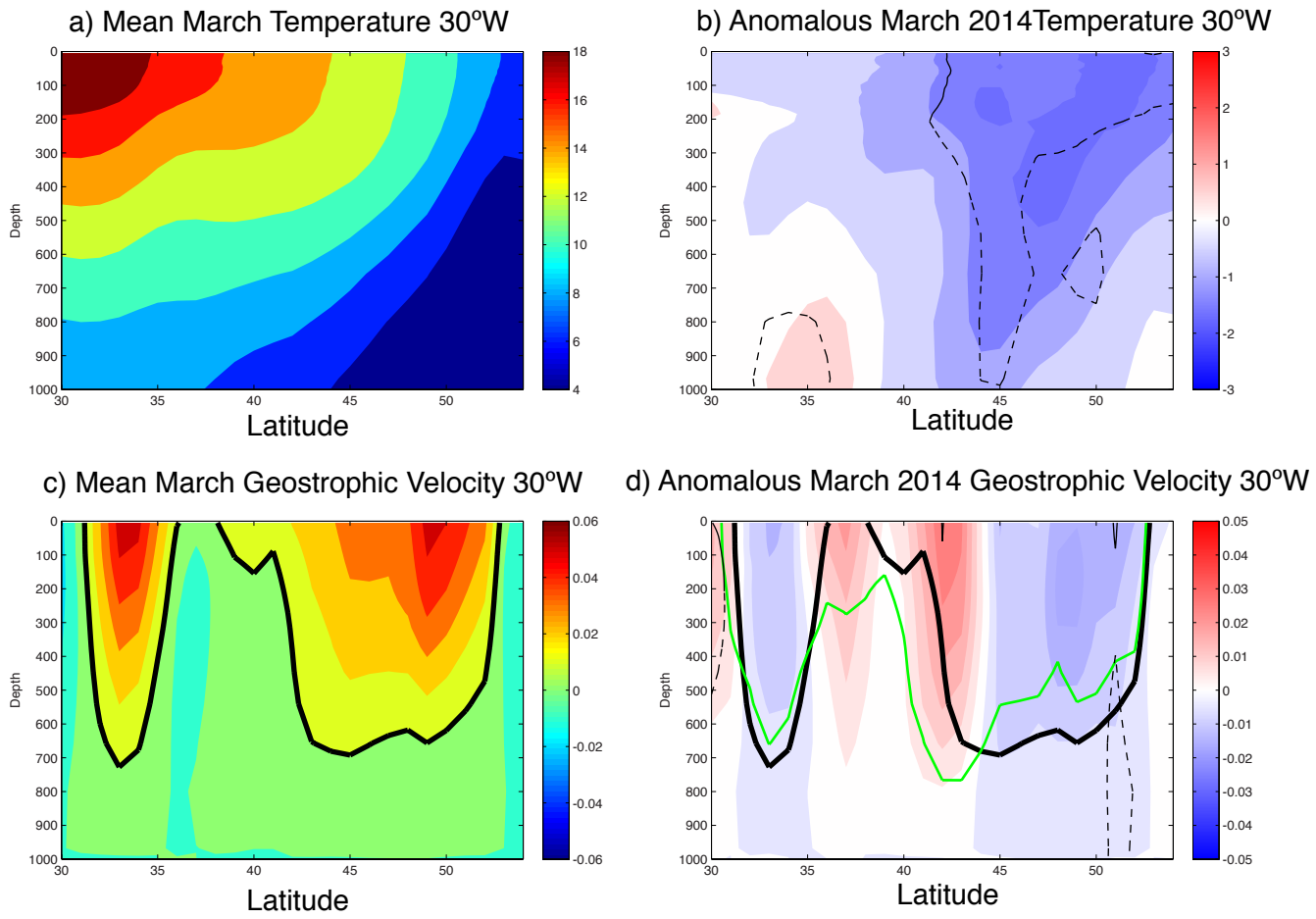

a) Mean March Temperature 30ºW
b) Anomalous March 2014Temperature 30ºW
c) Mean March Geostrophic Velocity 30ºW
d) Anomalous March 2014 Geostrophic Velocity 30ºW
Depth
Latitude
0
100
200
300
400
500
600
700
800
900
1000
30
35
40
45
50
18
16
14
12
10
8
6
4
3
2
1
0
-1
-2
-3
0.06
0.04
0.02
0
-0.02
-0.04
-0.06
0.05
0.04
0.03
0.02
0.01
0
-0.01
-0.02
-0.03
-0.04
-0.05

Figure 12

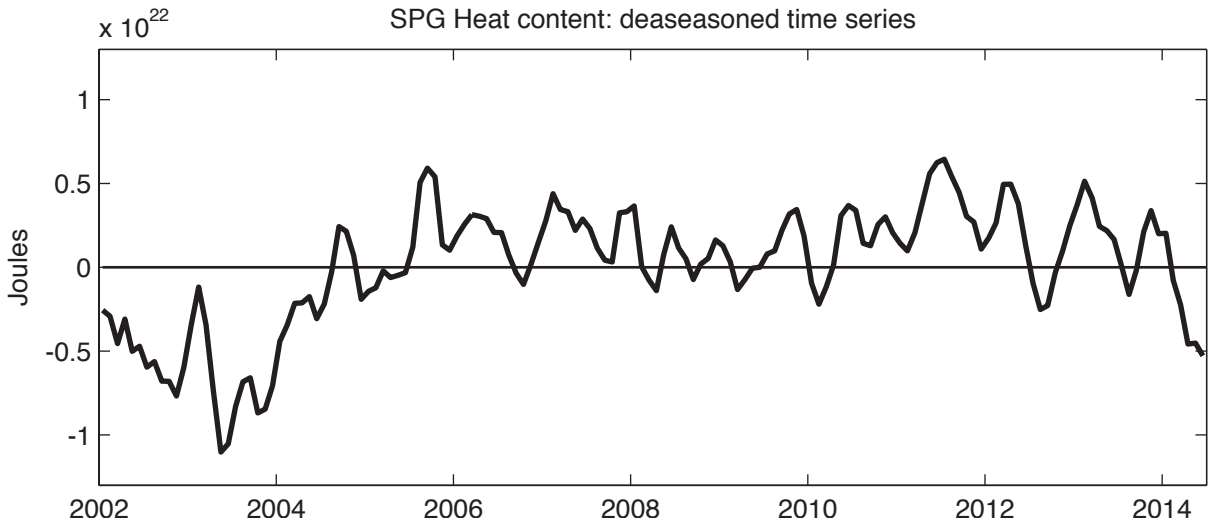

SPG Heat content: deaseasoned time series
x 10^22
Joules
1
0.5
0
-0.5
-1
2002
2004
2006
2008
2010
2012
2014

Figure 13

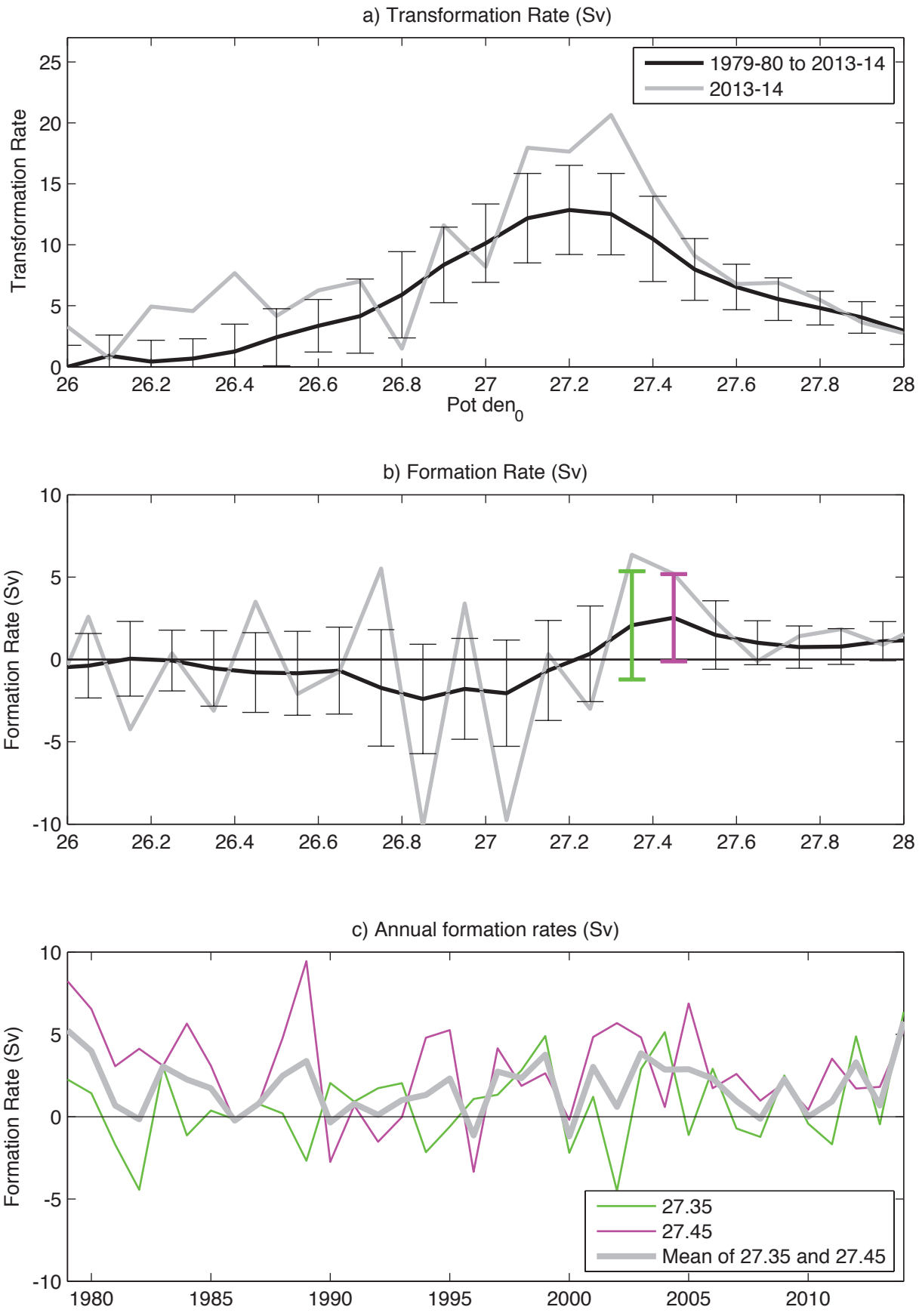

a) Transformation Rate (Sv)
1979-80 to 2013-14
2013-14
Transformation Rate
Pot den0
b) Formation Rate (Sv)
Formation Rate (Sv)
c) Annual formation rates (Sv)
Formation Rate (Sv)
27.35
27.45
Mean of 27.35 and 27.45

Figure 14

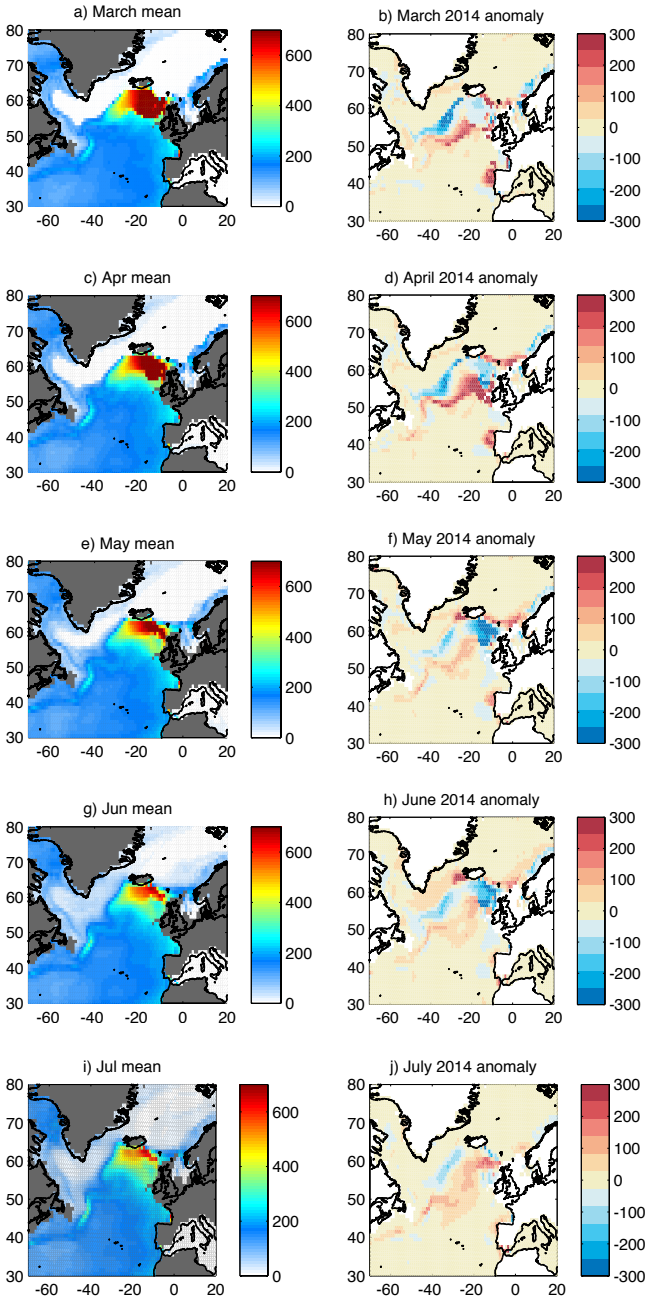

a) March mean
b) March 2014 anomaly
c) Apr mean
d) April 2014 anomaly
e) May mean
f) May 2014 anomaly
g) Jun mean
h) June 2014 anomaly
i) Jul mean
j) July 2014 anomaly
80
70
60
50
40
30
-60
-40
-20
0
20
600
400
200
0
300
200
100
0
-100
-200
-300

Figure 15

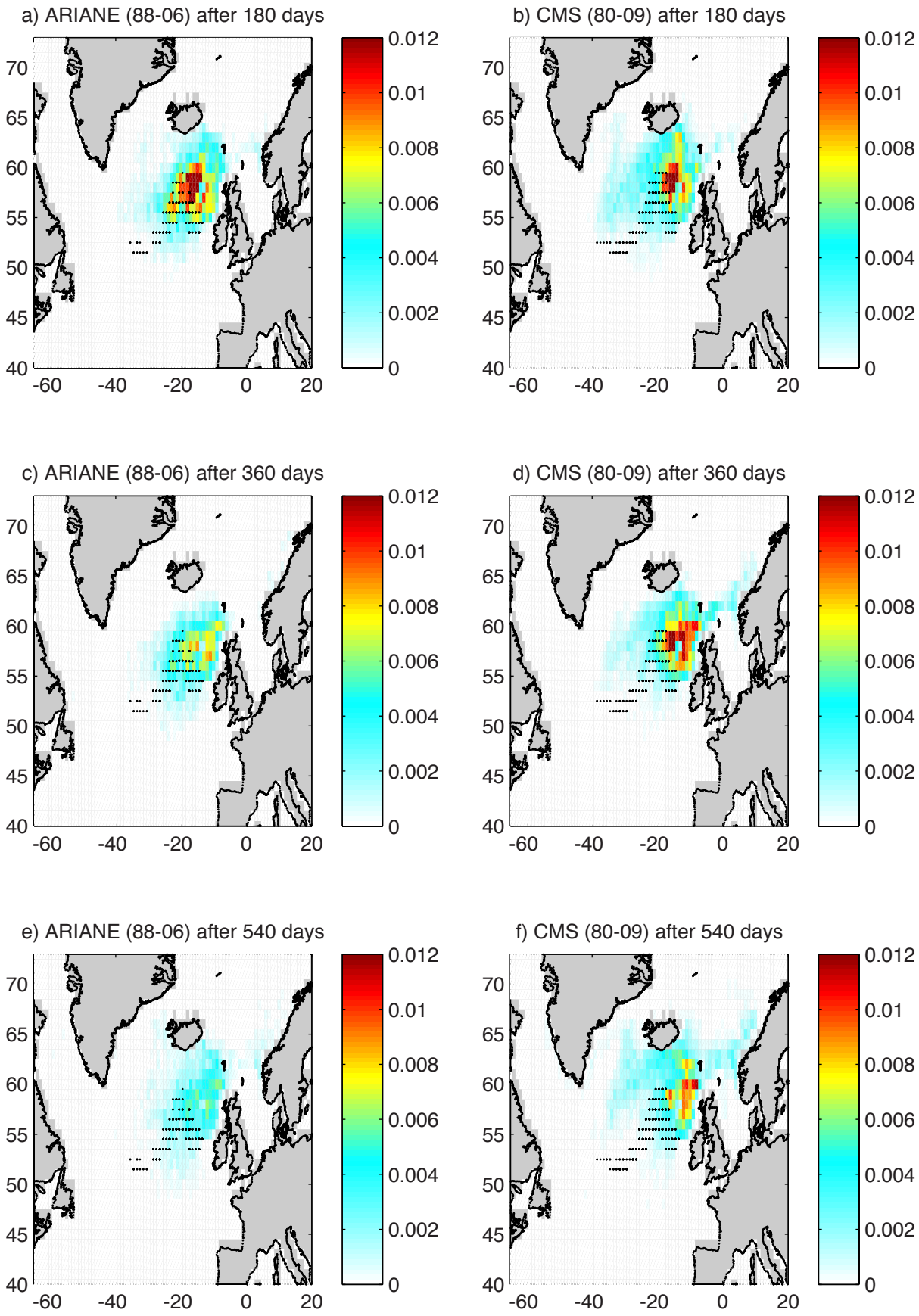
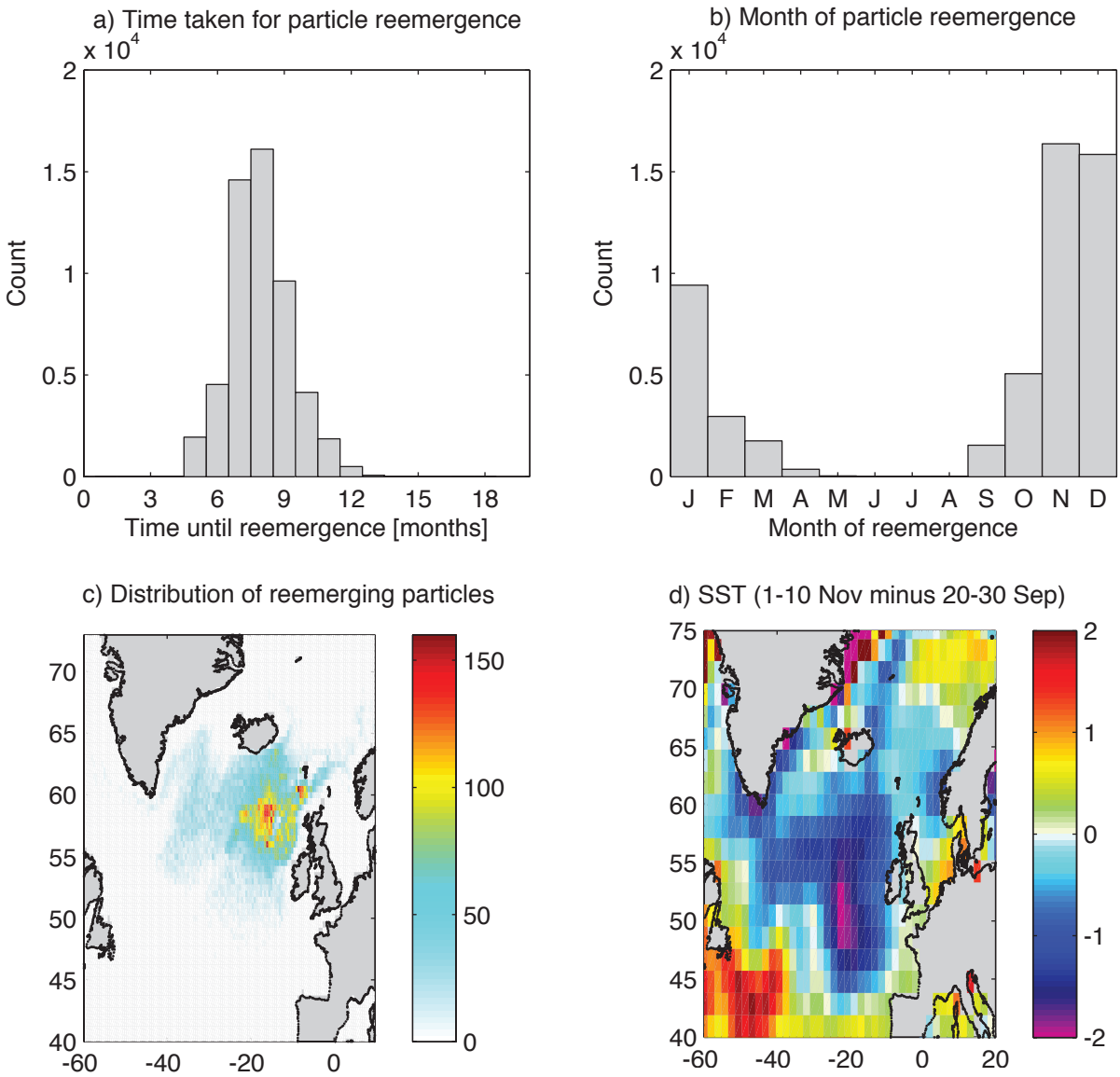

a) ARIANE (88-06) after 180 days
b) CMS (80-09) after 180 days
c) ARIANE (88-06) after 360 days
d) CMS (80-09) after 360 days
e) ARIANE (88-06) after 540 days
f) CMS (80-09) after 540 days
70
65
60
55
50
45
40
-60
-40
-20
0
20
0.012
0.01
0.008
0.006
0.004
0.002
0

Figure 16


a) Time taken for particle reemergence
x 10^4
Count
Time until reemergence [months]
b) Month of particle reemergence
x 10^4
Count
J F M A M J J A S O N D
Month of reemergence
c) Distribution of reemerging particles
d) SST (1-10 Nov minus 20-30 Sep)